Physics of the Earth and Planetary Interiors 311 (2021) 106643

Contents lists available at ScienceDirect

Physics of the Earth and Planetary Interiors

journal homepage: www.elsevier.com/locate/pepi

Upper crustal velocity structure of the Ailaoshan-Red River shear zone and its implication for Cenozoic tectonic-magmatic activity: Evidence from ambient noise tomography using short-period dense seismic array

Mengjie Zheng [a,b], Zhiming Bai [a,*], Tao Xu [a,c,**], José Badal [d]

[a] State Key Laboratory of Lithospheric Evolution, Institute of Geology and Geophysics, Chinese Academy of Sciences, Beijing 100029, China
[b] University of Chinese Academy of Sciences, Beijing 100049, China
[c] CAS Center for Excellence in Tibetan Plateau Earth Sciences, Beijing 100101, China
[d] Physics of the Earth, Sciences B, University of Zaragoza, Pedro Cerbuna 12, Zaragoza 50009, Spain

ARTICLE INFO

Keywords:
Dense short-period array
Ambient noise tomography
Cenozoic magmatism
Ailaoshan-Red River shear zone

ABSTRACT

The southern part of the Ailaoshan-Red River shear zone (ARRSZ) in southern Yunnan, is an important gold-bearing polymetallic metallogenic belt of China. To better understand the metallogenic tectonic setting and the magmatic activity in the area, we deployed a 240-km-long quasi-linear seismic array with numerous short-period stations spaced about 500 m across the ARRSZ. The shear-velocity structure of the upper crust along the survey profile is determined by ambient noise tomography using continuously recorded waveform data. The results show: (1) An upper crust characterized by a laterally varying S-velocity pattern and two high velocity bodies: one located mainly below the Ailaoshan metallogenic belt and the other further east below the Pingbian area, which are separated by a low velocity zone beneath the Red River Fault. (2) The upper crust model provides valuable information on Cenozoic magmatism. The high-velocity body below the Ailaoshan metallogenic zone likely corresponds to buried granitoid intrusions caused by early-stage Cenozoic magmatism, which might have been altered and mineralized. The high-velocity body near Pingbian could be the trace of basalt-generating late-stage Cenozoic magmatism, which is most likely the intrusive phase of the younger basalts. (3) Major regional faults are identified as ascending channels and/or emplacement/precipitation sites for magma and mineralized fluids, meaning that such faults play an ore-controlling function within the magmatic fluid ore-formation system.

1. Introduction

The Ailaoshan-Red River shear zone (ARRSZ), which lies on the southeastern margin of the Tibetan Plateau, is believed to be the tectonic boundary of the extruding Indochina block during the India-Eurasia collision (Peltzer and Tapponnier, 1988; Tapponnier et al., 1990; Tapponnier et al., 1986; Tapponnier et al., 1982). Along the ARRSZ, several metamorphic massifs (e.g., Ailaoshan) preserved abundant information on the thermal and tectonic evolution of the shear zone (Liu et al., 2012). High-potassium alkaline magmatic rocks are widespread throughout the shear zone (Liu et al., 2019), and this led to a series of studies on the genetic link between magmatic activity and ductile shearing (Leloup et al., 1995; Liang et al., 2007; Schärer et al., 1994). Furthermore, based on geological (Leloup et al., 1995; Tapponnier et al., 1982) and geophysical (Huang et al., 2002; Lei et al., 2009; Wang et al., 2014b; Zheng et al., 2014), the shear zone was generally assumed to be a deep fault zone rooted in the lithospheric mantle.

In the southern part of the ARRSZ, there are many porphyry-type copper-gold (e.g., Tongchang and Habo) and gold deposits (e.g., Daping and Chang'an), which are essential part of the lateral collision metallogenic belt of the Tibetan Plateau (Fig. 1). Much attention has been paid to the genetic mechanism and dynamic background of these deposits. The most representative point of view is that these deposits are mainly related to the magma or hydrothermal upwelling caused by the crustal tension movement during the Cenozoic (Cong et al., 2013; Ge et al., 2009; Tian et al., 2014; Yuan et al., 2010; Zhu et al., 2009). However, this assertion, made mainly by geologists and/or mineralogists, still needs confirmation due to the lack of robust evidence,

* Corresponding author.
** Corresponding author at: State Key Laboratory of Lithosphere Evolution, Institute of Geology and Geophysics, Chinese Academy of Sciences, Beijing 100029, China.
E-mail addresses: bbzzmm@mail.iggcas.ac.cn (Z. Bai), xutao@mail.iggcas.ac.cn (T. Xu).

https://doi.org/10.1016/j.pepi.2021.106643
Received 16 September 2020; Received in revised form 3 January 2021; Accepted 6 January 2021
Available online 12 January 2021

especially geophysical evidence.

In the Ailaoshan area, since the great collision between the Indian and Eurasian plates occurred at ca. 65 Ma (Peltzer and Tapponnier, 1988; Tapponnier et al., 1990; Tapponnier et al., 1986; Tapponnier et al., 1982), there has been significant rotation and extrusion or escape of blocks along the major strike-slip fault system. This has caused a migration of the deep material underlying the Tibetan Plateau to the surrounding areas, accompanied by massive magmatism (Xu et al., 2020). Previous studies suggest that Cenozoic magmatic activity in the region can roughly be sorted into two stages. The first stage of magmatism occurred mainly during 42–24 Ma and is characterized by epiphytic-ultra epiphytic alkali-rich porphyry intrusions associated with the aforementioned copper and gold deposits (Chung et al., 1998; Deng et al., 1998a; Deng et al., 1998b; Wang et al., 2001), which are widespread in the northern and middle sections of the ARRSZ. The second stage of magmatism took place after 17 Ma and is represented by the Cenozoic basalts exposed in the southeastern part of the shear zone (Huang et al., 2013b), for example in Pingbian, Maguan and northern Vietnam.

To date there have been numerous geophysical studies related to the ARRSZ (Bai and Wang, 2004; Bao et al., 2015a; Bao et al., 2015b; Cai et al., 2016; Hu et al., 2005; Huang et al., 2002; Li et al., 2014; Wang et al., 2003; Wang et al., 2014b; Wang et al., 2001; Xu et al., 2005; Yang et al., 2017; Zhang et al., 2020a; Zhang et al., 2011; Zhang et al., 2006; Zheng et al., 2014). However, the resolution of these geophysical surveys, usually performed with widely separated permanent seismic stations, is insufficient to reveal the detailed structure of the crust in the ARRSZ and adjacent areas. Hence, our main objective is to explore the fine structure of the upper crust and shed light on the relationship between the tectono-magmatic activity and the mineralization of Cu-Au and the deep structures south of the ARRSZ. To do this, due to the rugged topography and low road traffic, we deployed a dense quasi-linear seismic array oriented roughly west to east. Using continuously recorded waveform data, we first carry out ambient noise tomography to determine the shear velocity structure of the upper crust below the profile and then discuss the link between the crust model and magmatism and mineralization in the area of interest.

2. Geological setting

Our seismic profile spans several tectonic units, including the Lanping-Simao Basin (to the west), ARRSZ (middle transect), and South China Block (to the east). These structures are bounded/separated from west to east by the Jiujia-Anding Fault (JJ-ADF), Ailaoshan Fault (ALSF), and Red River Fault (RRF), respectively (Fig. 1). The ARRSZ extends to the southeast along the Ailaoshan Mountains and is bounded by the RRF to the east and the ALSF to the west. Within the southern area of the ARRSZ, there are a large amount of Cenozoic alkali-rich intrusive rocks, composed of shallow alkali-rich intrusions and alkaline volcanic rocks of eruptive phase (Ma et al., 2020). The left-lateral displacement of the ARRSZ has been estimated at ~500 km, but also at 700 ± 200 km or even more than 1000 km, from geological and paleomagnetic studies (Chung et al., 1997; Leloup et al., 1995; Tapponnier et al., 1982; Yang et al., 2001). The Red River Fault, which is interpreted to be the collision boundary of India with Eurasia (Tapponnier et al., 1990; Tapponnier et al., 1982), plays a key role in the extrusion, rotation and escape processes that affect the southeast margin of the Tibetan Plateau. The Ailaoshan Fault is the northeast boundary of the Lanping-Simao Basin and is probably the main structure that controls the regional mineralization because many polymetallic and gold deposits are distributed on both sides of this fault or its branches (e.g., the Ganhe Fault).

Typical deposits in the southern part of the ARRSZ, such as the porphyry Cu-(Mo-Au) deposit of Habo, the Au-Cu deposit of Chang'an, the Cu-Au polymetallic deposit of Tongchang and the Au-polymetallic deposit of Daping, can be classified into two groups (Ge et al., 2010). One is of porphyry type (Tongchang, Habo) and hydrothermal alteration type (Chang'an), both related to the alkali-rich intrusive rocks of the Himalayan stage. The other is of quartz-vein type and limonite-vein type (Daping), related to the intermediate-acid and alkali-rich magmatic activity during the Indosinian tectonism, the Yanshanian movement and the Himalayan orogeny. These metallic deposits of distinct types and combinations of elements were formed in the course of different evolutionary stages of tectonic magma, which result from superposition of mineralization activities related to multiphase tectonic magmatic activities (Ge et al., 2010).

3. Data acquisition and noise correlation functions

Passive source detection technology based on a dense short-period seismic array is widely used in recent years and is a way to obtain enough information to explore deep structures, with the advantage of being environmentally friendly, low-cost, and capable of providing high-resolution results (Zhang et al., 2020b). In order to investigate the main mineral deposits and geological units mentioned above, even though the study area is located in a mountainous zone in southern Yunnan that has a rugged topography and poor traffic conditions, we deployed a 240-km-long quasi-linear array with short-period seismic stations at intervals of about 500 m (Fig. 1) and collected continuous ambient noise data over a 35-day time interval, from December 2017 to January 2018. In what follows, we perform ambient noise tomography

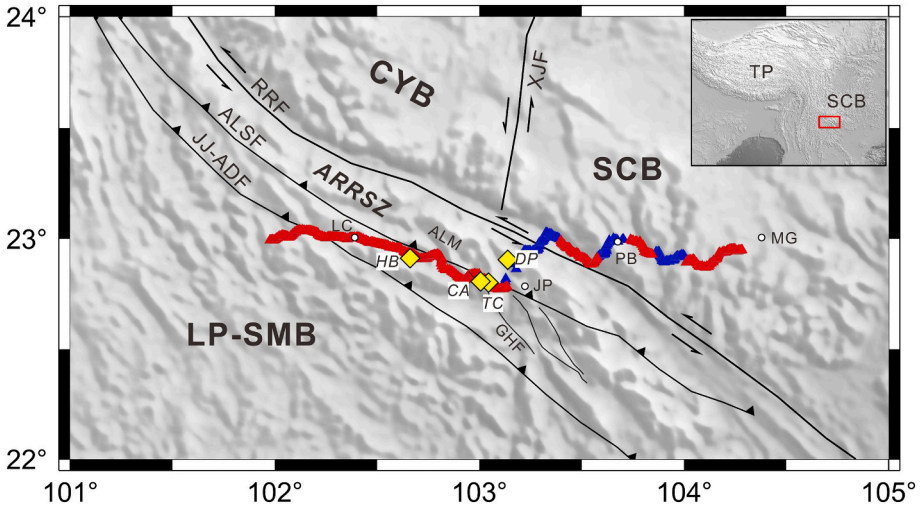

Fig. 1. Tectonic blocks, faults, and seismic stations on a topographic map of the study area. The small rectangle in the right upper inset delimits the study region. Triangles show the locations of the seismic stations: PDS-2 instruments (in red); EPS instruments (in blue). Yellow diamonds mark ore deposit locations. Acronyms: JJ-ADF, Jiujia-Anding Fault; ALSF, Ailaoshan Fault; RRF, Red River Fault; XJF, Xiaojiang Fault; GHF, Ganhe Fault; LP-SMB, Lanping-Simao Basin; ARRSZ, Ailaoshan-Red River shear zone; ALM, Ailao Mountain; CYB, Central Yunnan Block; SCB, Sichuan Basin; TP, Tibetan Plateau; HB, Habo ore deposit; CA, Chang'an ore deposit; TC, Tongchang ore deposit; DP, Daping ore deposit; LC, Lvchun; JP, Jinping; PB, Pingbian; MG, Maguan. (For interpretation of the references to color in this figure legend, the reader is referred to the web version of this article.)

with the help of a short-period dense seismic array, which is a widely used method in recent years (Badal et al., 2013; Fang et al., 2015; Li et al., 2016a; Li et al., 2016b; Liu et al., 2018; Roux et al., 2016).

First, the continuous waveforms in both PDS and MiniSEED format were converted to the common SAC format. In this study, we only used vertical component data. Then, the continuous seismic recordings were cut into 1-h segments to ensure a certain amount of information for its later stacking. For the sake of compatibility and efficient computational cost reduction, the data were resampled at a rate of 10 Hz. All individually recorded waveforms were systematically pre-processed following the procedure of Bensen et al. (2007), including removing of the instrument response, detrending the zero-line slope, band-pass filtering in the 0.75–12 s bandwidth, spectral whitening, and temporal normalizing for the data.

After completing the preprocessing steps above, the time domain ambient noise cross-correlation $C_{AB}(t)$ between station A and B is calculated as follows:

$$C_{AB}(t) \approx \int_0^{t_c} v_A(\tau) v_B(t+\tau) d\tau$$

where $v_A(t)$ and $v_B(t)$ are the continuously recorded data at stations A and B, respectively. In this study, the lag time t between $v_A(t)$ and $v_B(t)$ shifts from −50 to 50s, and t_c is the length of the time segment used for cross-correlation, which is one hour in this case. The final noise correlation functions (hereafter NCFs) of a single pair of stations were obtained by linearly stacking all hourly cross-correlations.

Fig. 2 shows an example record section of cross correlations between a virtual source station 1040 and all receiver stations. We can observe the emergence of surface wave signals clearly. However, the signal-to-noise ratio (SNR) for periods of 1–2 s is relatively low (Fig. 2a). This may be because the profile is close to the highway, so the higher frequencies could be affected. On the other hand, the irregular topography of the study area can also affect the high frequency signals. Considering a high SNR, as well as the corner frequency of the instruments, we take the period band of 1–5 s (0.2–1 Hz) as the range to extract the surface-wave velocity dispersion.

4. Rayleigh wave dispersion measurement

Surface-wave group velocity dispersion can be estimated from the NCFs (Sabra et al., 2005b; Shapiro and Campillo, 2004) and the time-domain empirical Green functions (EGFs) given by the time derivative of the NCFs (Sabra et al., 2005a; Sabra et al., 2005b). Yao et al. (2006) demonstrated that phase velocity dispersion curves can also be measured from the EGFs. Here we extracted Rayleigh wave phase velocity dispersion curves from the EGFs of each station pair using the method by Yao et al. (2006), based on a far-field representation of the Green's function and an image transformation technique (Yao et al., 2005).

In order to satisfy the far-field approximation (Luo et al., 2015; Yao et al., 2011), we required that the interstation distance is at least greater than 1.5 times the wavelength. Given the large amount of data to handle, we only took a SNR threshold of 5 as the criteria and automatically extracted the phase-velocity dispersion curves, then applied quality control measures to the dispersion data to identify and reject incorrect measurements.

To avoid the 2π ambiguity while picking phase dispersion curves, we adopted additional precautions. (1) We optimized the initial phase velocity model iteratively after each automatic extraction. (2) Following Bonadio et al. (2018), we summed all branches of the entire families of possible phase-velocity curves (including those affected by the 2π ambiguity) in the entire 1–5 s range. This provides a density distribution graph (Fig. 3) with a stack of all the measurements in the period range of interest. With measurements from different interstation pairs stacked together, we obtained the local-average dispersion curve, which can help us optimize the reference phase-velocity model.

4.1. Topographic effect

The profile stretches across southern Yunnan through a mountainous area with rugged topography. The average altitude at which the array stations were installed is 923.89 m, with 1940 m and 134 m being the maximum and minimum elevations, respectively. In theory, the

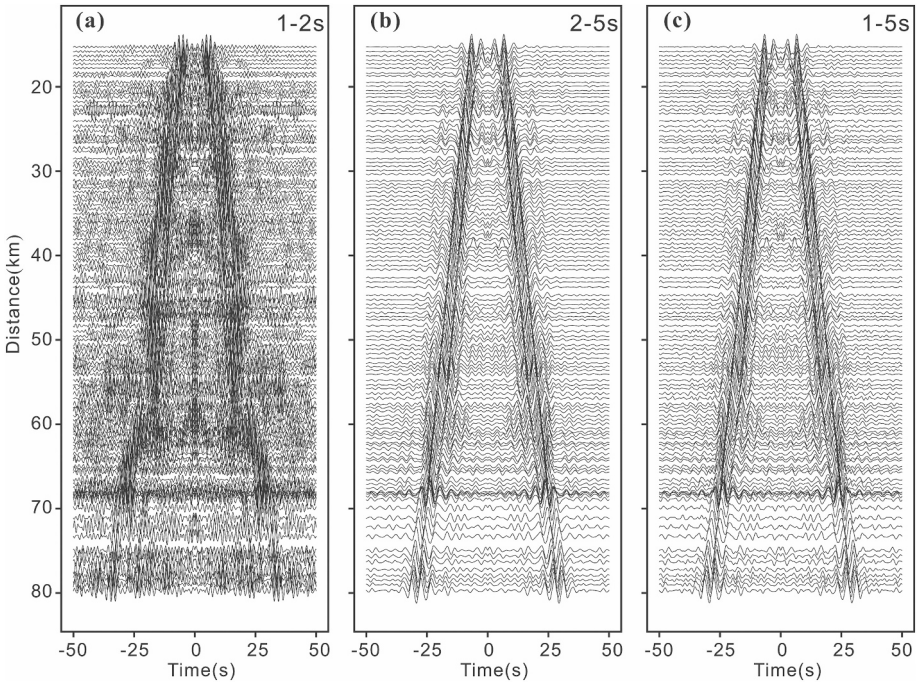

Fig. 2. Cross-correlations of the vertical component signal recorded at station 1040 with the signals recorded at all other stations, against the distance between stations. Plots for three different period ranges: (a) 1–2 s; (b) 2–5 s; (c) 1–5 s. Horizontal axis is time (s) and vertical axis is interstation distance (km). Positive and negative signals are processed symmetrically.

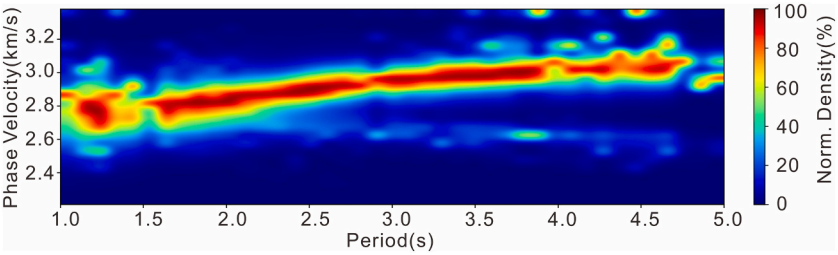

Fig. 3. Density distribution graph obtained by stacking all preliminary phase-velocity dispersion curves, once normalized to the maximum for each period within the 1–5 s range. The stacked measurements involve all phase-velocity dispersion curves (including those affected by the 2π ambiguity) for all pairs of stations.

difference in topographic elevation between pairs of stations could affect the Rayleigh-wave phase-velocity dispersion measurements (Huang et al., 2017; Huang et al., 2018). To evaluate the influence of topography, we used the analysis method of Huang et al. (2017). The distance between pairs of stations is $d_L = \sqrt{d_H^2 + d_V^2}$, where d_H is the horizontal interstation distance and d_V is the difference in topographic elevation. Starting from these distances d_H and d_V, we took into account the absolute difference $\Delta d = d_L - d_H$ and the relative difference $\Delta d/d_L$. The absolute difference Δd is extremely small, lower than 20 m in 94.3% of station pairs, while the relative difference $\Delta d/d_L$ is less than 0.1 in 97.49% of station pairs (Table 1). The topographic effect on dispersion measurements is small or negligible as long as the difference between d_H and d_L is small. Ultimately, we thus adopted the criterion $\Delta d/d_L < 0.1$ used to retain the phase velocity dispersion curve for further processing.

4.2. Cluster analysis

For short periods, the smoothness and continuity of the dispersion curves are good criteria to evaluate the validity of the phase velocity determinations (Ekström et al., 2009). However, these criteria are difficult to implement in practice. If only the smoothness and continuity of the dispersion curves are considered, it's very likely that abnormal measurements reflecting real subsurface structure will be rejected, especially when dealing with complex study areas. Inspired by the cluster measurements performed by Bensen et al. (2007), we adopted the concept of similar path to carry out cluster analysis in the context of a short-period dense seismic array, paying attention to the stability and coherence of spatial clusters.

Clustering measurements are commonly used to assess uncertainties and to identify outliers in earthquake dispersion measurements. Dispersion curves obtained from similar paths are clustered to reduce redundancy and assign uncertainty estimates (Ritzwoller and Levshin, 1998). A similar analysis method can be applied to ambient noise data (Bensen et al., 2007) and performed when a tight cluster of stations subtends a small angle to a relatively distant station (located many interstation spacings away from the cluster).

In this study, given a source station and a receiver station, all other nearby stations within a circle of radius r form a source station cluster and a receiver station cluster, respectively, in such a way that it can be considered that all pairs of stations formed by any two of them from each cluster define a similar interstation seismic path. Fig. 4 illustrates this concept, where D is the interstation distance and r is the radius (distance) that meets the similar path requirement. In our implementation, we took $r = D/n$, and the rule of thumb states that n is an integer between 6 and 10.

After determining the similar path for each individual dispersion curve, we performed cluster analysis with all the dispersion curves obtained from a same similar path. Here we evaluated the stability and coherence of the clustered dispersion curves, taking as reference the average dispersion curve and the standard deviation for each period, which allows us to identify and reject poor measurements. Specifically, for each period, we kept the measurements within 2 standard deviations and considered data points outside this range as dispensable. If the number of bad points exceeds 50% of the original data points, the dispersion curve is rejected. By this procedure, we obtained a total of 29,417 phase-velocity dispersion curves. The average standard deviation decreases from 0.093 to 0.074 after quality control of the data, and although the number of paths involved in the dispersion measurements for different periods decreases, it still exceeds almost 15,000 (Fig. 5).

Table 1
Statistical figures related to the topography and location of the array stations.

Δd(m)	0–10	10–20	20–40	~40
Number of pairs of stations	27,517	5298	1810	174
Percentage (%)	79.08	15.22	5.20	0.50
$\Delta d/d_L$(%)	0–0.1	0.1–0.2	0.2–0.4	~0.4
Number of pairs of stations	33,925	708	165	1
Percentage (%)	97.488	2.035	0.474	0.003

$\Delta d = d_L - d_H$ is the absolute difference between the distance d_L and the horizontal distance d_H between pair of stations, while $\Delta d/d_L$ is the relative difference.

5. Inversion for shear velocity

In contrast to the classical two-step surface-wave inversion method, Fang et al. (2015) proposed direct inversion of surface-wave dispersion data for 3-D shear wave velocity structure. This method is based on frequency-dependent ray tracing and wavelet-based sparsity-constrained tomography. Taking into account the effect of ray bending in surface wave tomography in a complex medium, this method is suitable for a shallow complex region where the great-circle hypothesis is not satisfied. In this study, we used the direct inversion method proposed by Fang et al. (2015) to resolve the shear wave velocity structure beneath the profile.

5.1. Construction of an initial 1D velocity model

Following Shearer (2019), we constructed an initial 1-D shear-wave velocity model directly from the available dispersion data. We converted

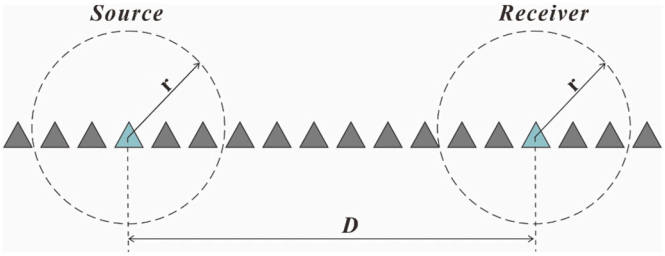

Fig. 4. Schematic representation illustrating the definition of similar seismic path. The colored triangles represent the source station and the receiver station to correlate the ambient seismic noise and calculate a single shear-velocity dispersion curve. D is the interstation distance and r is the radius (distance) that geometrically meets the similar path requirement (see main text).

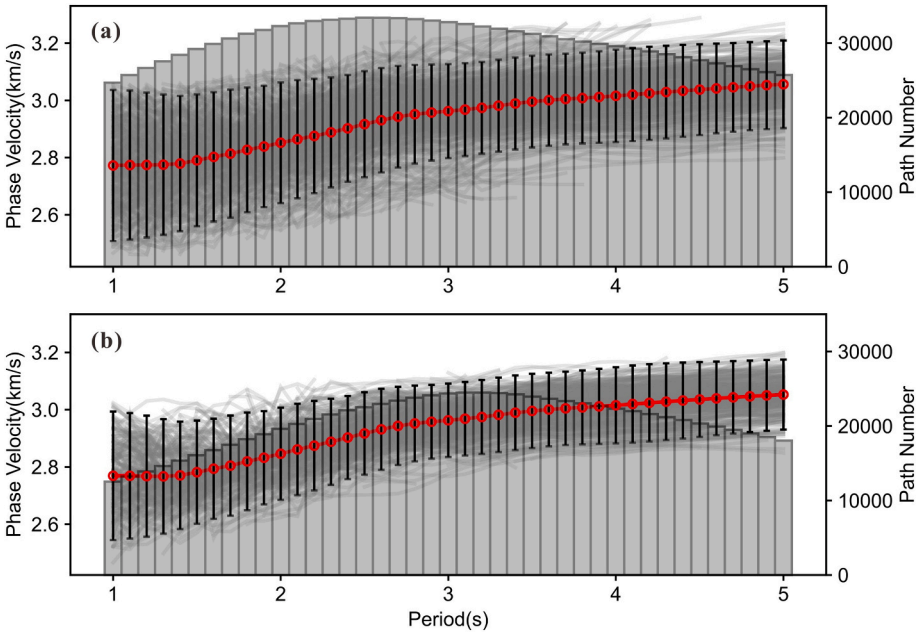

Fig. 5. Rayleigh phase velocities before (a) and after (b) quality control. The solid gray lines are 500 randomly picked dispersion curves. The red circles indicate average phase velocity values for periods within the 1–5 s interval, which draw the local-average dispersion curve. Error bars indicate twice the standard deviation. The bar histograms show the number of seismic trajectories involved in the dispersion measurement for different wave periods. X axis is for periods and Y axis is for phase velocity (left) and path number (right). (For interpretation of the references to color in this figure legend, the reader is referred to the web version of this article.)

each data point of the period-dependent phase-velocity dispersion curve into a point of the depth-dependent shear velocity model, taking the shear velocity as 1.1 times the phase velocity and the depth as 1/3 of the corresponding wavelength. After converting all dispersion curves into velocity-depth models, we averaged all these curves to obtain a priori information on shear velocity at depths of 1 to 5 km (small gray circles at shallow depths in Fig. 6a). For the sake of the stability for inversion, the maximum depth for inversion was set at 16 km, to which we assigned the shear velocity value of 3.55 km/s according to previous studies. The value of the shear velocity on the surface is set to 2.90 km/s (Fig. 6a). From here, the initial 1-D shear velocity model was then constructed by interpolation from a given depth sampling point, adopting 1-km-thick layers from 0 to 6 km and 2-km-thick layers at greater depths (Fig. 6b).

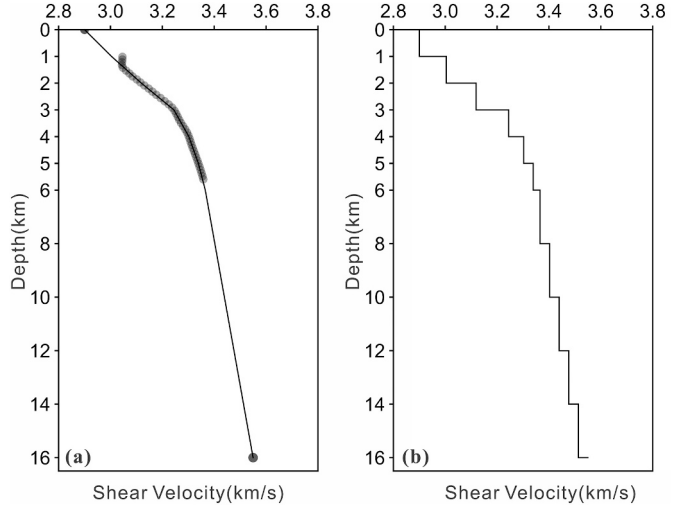

Fig. 6. Initial 1-D shear-velocity model: (a) Model based on a priori information obtained by direct conversion of dispersion curves into shear velocity-depth models. Small gray circles indicate a priori information on shear velocity at shallow depths (see main text). (b) Velocity-depth model consisting of 12 layers at increasing depths, obtained by interpolation and adopting layer thicknesses of 1 km from 0 to 6 km and of 2 km at greater depths down to 16 km.

5.2. Coverage of the scanned area

Obviously, the *E*-W-extending nature of the quasi-linear array means a dense ray coverage in longitude but poor coverage in latitude, which is also confirmed in ray path coverage density map obtained from the inversion result (Fig. 7). Therefore, we designed a mesh with an uneven grid spacing of 0.045° (about 5 km) in longitude and 0.09° in latitude. Otherwise, due to the irregular geometry of the short-period seismic array, the direct allocation of shear velocity below the stations could introduce a notable distortion of the results and therefore of the seismic image obtained from them. In what follows, we thus considered a virtual profile (red line in Fig. 7) following the survey geometry (gray triangles in Fig. 7) to get a vertical velocity section of the upper crust.

5.3. Upper crust shear-velocity image

Through the direct inversion of surface wave dispersion (Fang et al., 2015), we obtained the shear velocity structure beneath the aforementioned virtual profile (Fig. 8). Within the depth range explored, we observed a relatively low velocity zone below the RRF that contrasts with the higher velocities on both sides of this fault. The RRF separates two high velocity zones, one to the west and the other one to the east. To the east of RRF, the high-velocity body about 20 km wide occurs in the upper crust between 4 and 8 km depth. A little further east, there is a low velocity anomaly of relatively smaller lateral width within the same depth range. To the west of the RRF, that is, below the Ailaoshan metallogenic belt represented by the Habo, Tongchang and Daping ore deposits, there is a more extensive high-velocity zone below 4 km depth in the upper crust, which is composed of two perfectly distinguishable subzones on both sides of the longitude 103° (Fig. 8).

5.4. Assessment of the inversion results

5.4.1. Analysis of topography effect

Undoubtedly, the rugged topography has some influence on the dispersion measurement and inversion in ambient noise tomography. There is still no reputable and widely used solution, although some efforts have been made on this (Fu et al., 2017; Huang et al., 2017; Huang et al., 2018; Köhler et al., 2012; Koulakov et al., 2016; Matos et al., 2015; Wang et al., 2017). In this research, we first identified and rejected the

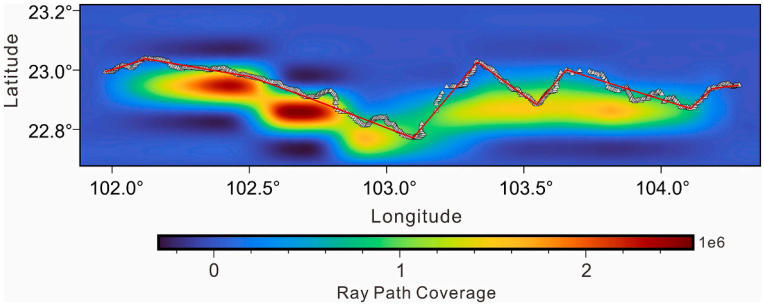

Fig. 7. Ray-path coverage density map showing the apparently scanned area. The virtual profile adopted for the calculation (red line) appears superimposed on the dense seismic array (gray triangles). (For interpretation of the references to color in this figure legend, the reader is referred to the web version of this article.)

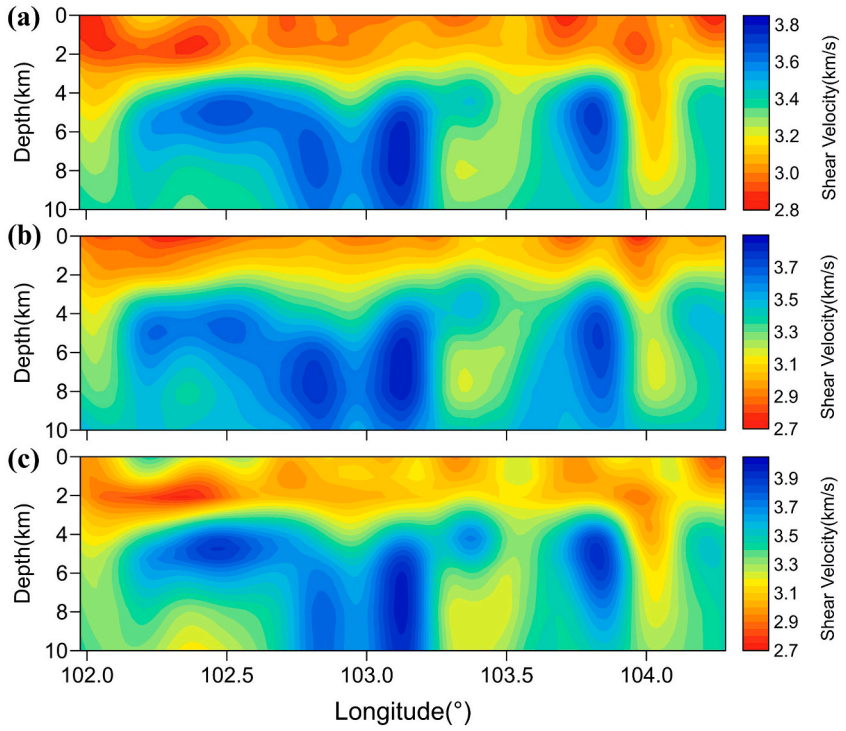

Fig. 8. Shear velocity sections (color scale on the right) along the virtual profile: (a) inversion result for periods of 1–5 s; (b) inversion result for periods of 2–5 s; (c) image based on the inversion of the average dispersion curves of each cluster corresponding to a similar path.

dispersion curves that could be greatly affected by topographic factors, following the procedure proposed by Huang et al. (2017). Bearing in mind that high-frequency data may be more the most affected, we performed inversion using the dispersion data in the period range of 1–5 s and then repeated the process from the data of 2–5 s. Fig. 8a and b show the respective results for comparison and as we can see they are quite similar.

Based on the concept of similar path, we inverted the average dispersion curves of each cluster corresponding to a similar path, that is, we took advantage of the cluster information referred to the dispersion curves after quality control. This gives us the opportunity to compare the results of prior inversions with those obtained through this procedure and thus check the consistency between them. Fig. 8c shows the equivalent image of the upper crust using clustered dispersion data within the 1–5 s period range. The image obtained is very similar to the previous ones, so the consistency of the tomograms shown in Fig. 8 supports the confidence in the structure of the upper crust determined here.

In addition, we used different initial velocity model to assess the constraint ability of depth of our 1–5 s dispersion data. Specifically, we adopted the same structure as mentioned in section 5.1, with 1-km-thick layers between 0 and 6 km and with 2-km-thick layers at greater depths. The difference is that these trial initial models have a constant velocity gradient of 0.05S-1 and a velocity range from 2.8–3.6 km/s at the surface (Fig. 9a). Using the same inversion procedure with non-clustered dispersion data within the 1–5 s, we obtained the 1-D velocity models corresponding to the five previous initial models for the grid points (102.38°E, 22.90°N) and (103.86°E, 22.90°N). These models reveal large differences at depths less than 2 km and greater than 10 km (Fig. 9b, c). This is not surprising when exploring a depth greater than 10 km, since in our case the dispersion data used for the inversion correspond to periods less than 5 s, which is theoretically related to the surface wave sensitivity kernels and leads to a loss of the ability to constrain deep structure. As for depths less than 2 km, although the dispersion data used for inversion vary from 1 to 5 s, the SNR of NCFs for the shortest periods (1–2 s) is low (Fig. 2a). Furthermore, the rugged topography also directly affects the measurement and inversion of the dispersion data referred to these short periods. Therefore, the results for depths less than 2 km may not be reliable.

According to all these factors, we adopted the inversion model using

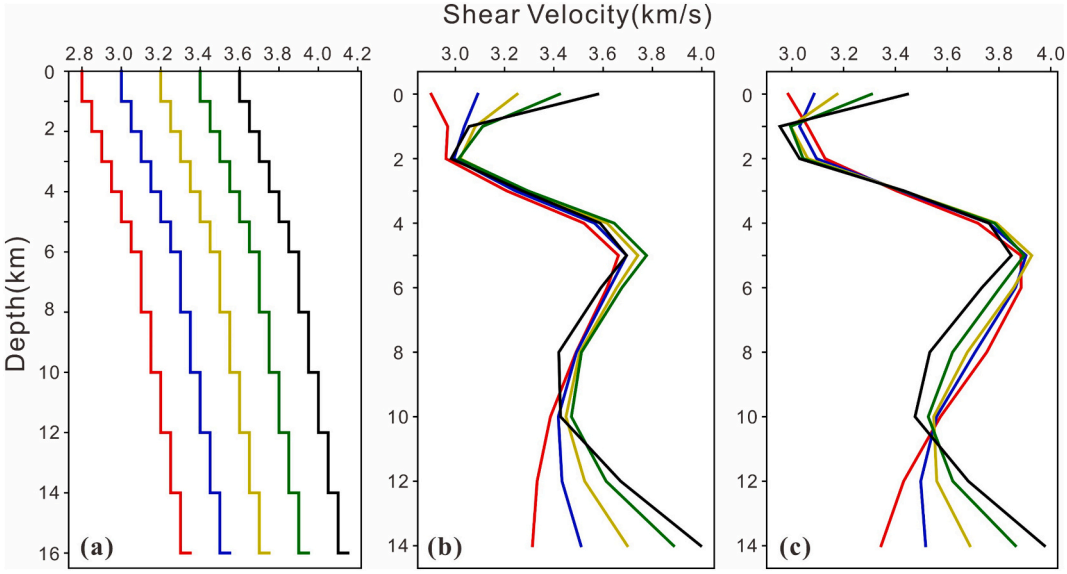

Fig. 9. (a) Initial trial models (characterized by different colors) that have the same velocity gradient; (b) inverted models from them (depicted by different colors) associated to the grid point (102.38°E, 22.90°N); (c) inverted models associated to the grid point (103.86°E, 22.90°N).

non-clustered dispersion data of 1–5 s and only focused on depths of 2–10 km range in subsequent discussion. Correspondingly, after our iterative and non-linear inversion, the average and standard deviation of the travel time residuals are 0.4 ms and 0.35 s, respectively, and the root mean square of the travel time residual decreases from 0.469 s to 0.372 s after iteration (Fig. 10).

5.4.2. Resolution test

To overcome difficulties in field operations and explore important mineral deposits and geological units as much as possible, the survey geometry of our pseudo-linear array in *E*-W direction is unusual. The ray coverage density map (Fig. 7) suggests that the ray paths mostly sample zones close to the pseudo-linear array. To test the model resolution under the current data distribution and inversion settings, we conducted an unusual checkerboard resolution test, which might be called 'piano-keyboard test' as it only deals with lateral (or in longitude) resolution. The input model consists of alternate velocity anomalies of ±0.4 km/s with a size of 0.18° (approximately 20 km) in longitude direction. Synthetic travel time data for the input model were calculated at each period using the same ray paths as in the real data. We added 2% random noise to the synthetic time data and inverted these data using the same inversion strategy as with real data. The results obtained reveal a recognizable velocity pattern near the array stations and for depths of 2 to 10 km (Fig. 11), although there is an obvious smearing effect when moving away from the array. The recovered amplitude near the pseudo-linear array is almost the same as the input value (±0.4 km/s) at the depths of 4, 6 and 8 km (Fig. 11c-e), but reduce a lot at the depth of 2 km (Fig. 11b) and 10 km (Fig. 11f), which is consistent with the conclusion deduced from different initial model test (Fig. 9). In practice, both tests provide the same depth limit for vertical resolution.

To check whether the vertical velocity section obtained from the virtual approach profile could introduce fake anomalies (artifacts) because of interpolation of data points, we presented the shear-wave velocity anomalies of our model for four horizontal planes at different depths of 4, 5, 6 and 8 km. The results can be viewed in Fig. 12 and show a good consistence with the feature revealed by the vertical velocity section (Fig. 8).

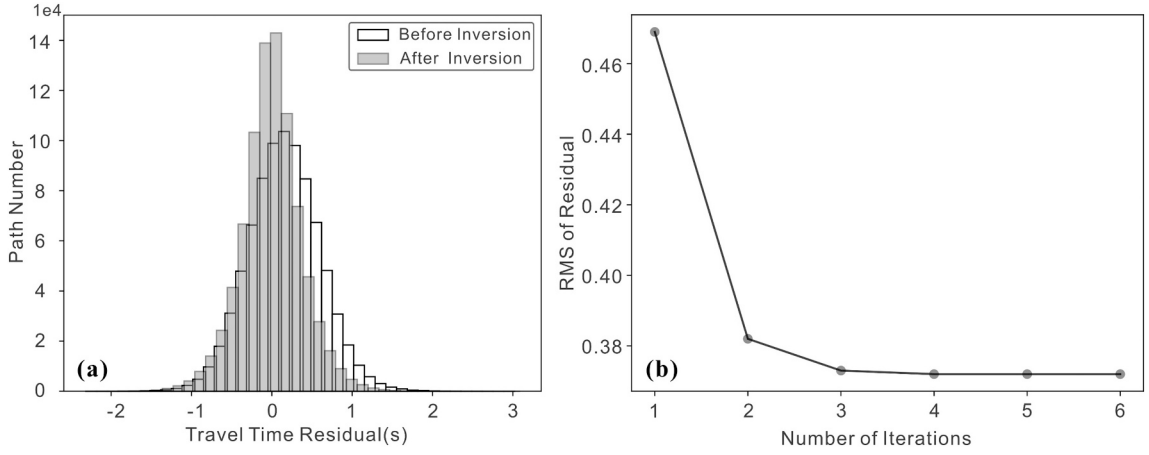

Fig. 10. The distribution of surface wave travel time residuals (a) and travel time residual curve along with iterations (b). In (a), the histogram of travel time residuals before the inversion is marked by unfilled black line and after the inversion is marked by filled black line.

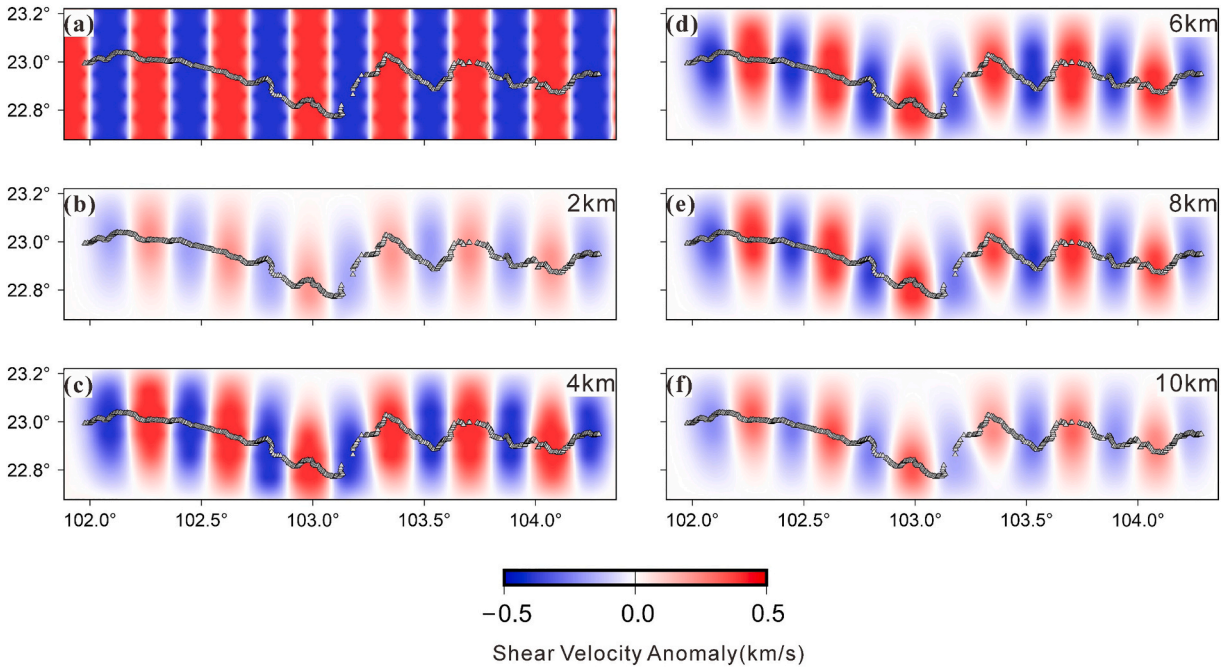

Fig. 11. Checkerboard test. (a) The input initial model consists of alternate velocity anomalies of ±0.4 km/s with a size of 0.18°in longitude direction. (b) – (f) Recovery of the checkerboard model at different depths of 2-10 km (see color scale at the bottom). The gray triangles show the location of the dense short-period seismic array deployed on the ground.

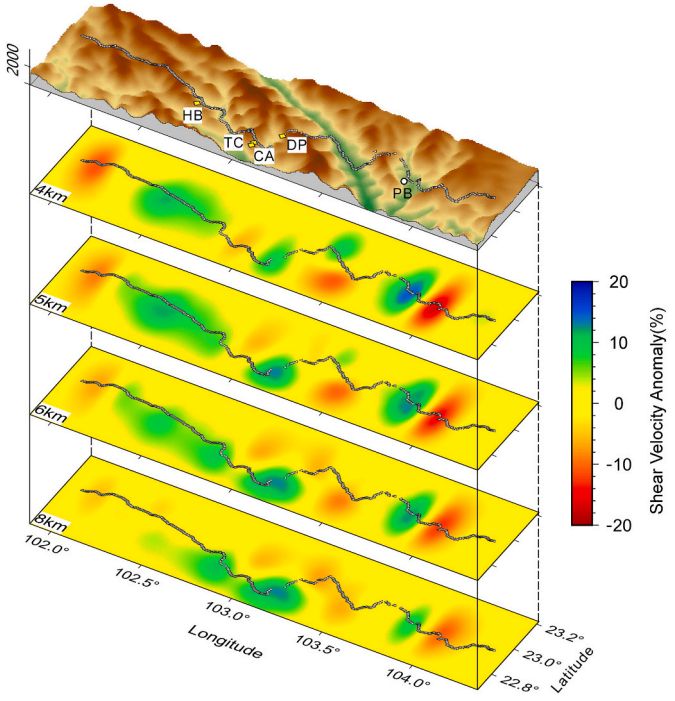

Fig. 12. Horizontal slices showing shear wave velocity anomalies (see color scale on the right) at different depths down to 8 km. In all cases, the wavy line traced by gray triangles shows the location of the dense short-period seismic array. Above these velocity sections is a 3D topographic map showing the respective locations of the ore deposits of Habo (HB), Tongchang (TC), Chang'an (CA), and Daping (DP), and Pingbian county (PB).

6. Discussion

6.1. Comparison with previous results

The upper crust model we have obtained reveals a laterally varying S-velocity pattern with alternating high and low velocities (Fig. 13d), which correlates well with the high and low fluctuations of the observed magnetic anomaly (black line in Fig. 13c). The analysis of the attenuation of different wavelengths with height (Lou and Wang, 2005; Wen et al., 2017) has demonstrated that short and medium wavelength anomalies overlap a weak magnetic field, suggesting a shallow crustal source as the cause of the fluctuations of the observed magnetic anomaly. In contrast, the Bouguer gravity anomaly varies quite irregularly (gray line in Fig. 13c), but approximately exhibits relatively low negative values (less than −40 mgal) west of the RRF and higher values just east of this fault.

The S-wave velocity model shows high velocity values below the ARRSZ (Fig. 13d), which is in agreement with previous P-wave velocity models obtained by other methods, such as body-wave tomography (Xu et al., 2005), joint local and teleseismic tomography (Lei et al., 2009) and stepwise inversion employing crustal P and Pn waves (Huang et al., 2013a). These models show high velocities in the upper and middle crust and low velocities in the lower crust and near the Moho beneath the ARRSZ. Xu et al. (2005) explained that the high velocities observed in the upper crust are the trace of the rapid uplift and cooling of the metamorphic belt after the ductile shearing of the fault zone, while the low velocities in the middle-lower crust imply a relatively active crust-mantle boundary beneath the fault zone. On the other hand, the high Vp/Vs ratio beneath the ARRSZ (Fig. 14b), determined from receiver functions using the same survey array (Zhang et al., 2020a), is probably an indicator of a relatively high proportion of ferromagnesian materials in the crust.

The low velocity zone beneath the Red River Fault, between two high-velocity zones on its both sides (Fig. 13d), seems to indicate a significant difference in lithology and mineral composition compared with both sides. Various studies of the anisotropy of the crust show different stress directions (Gao et al., 2012; Shi et al., 2012; Wang et al.,

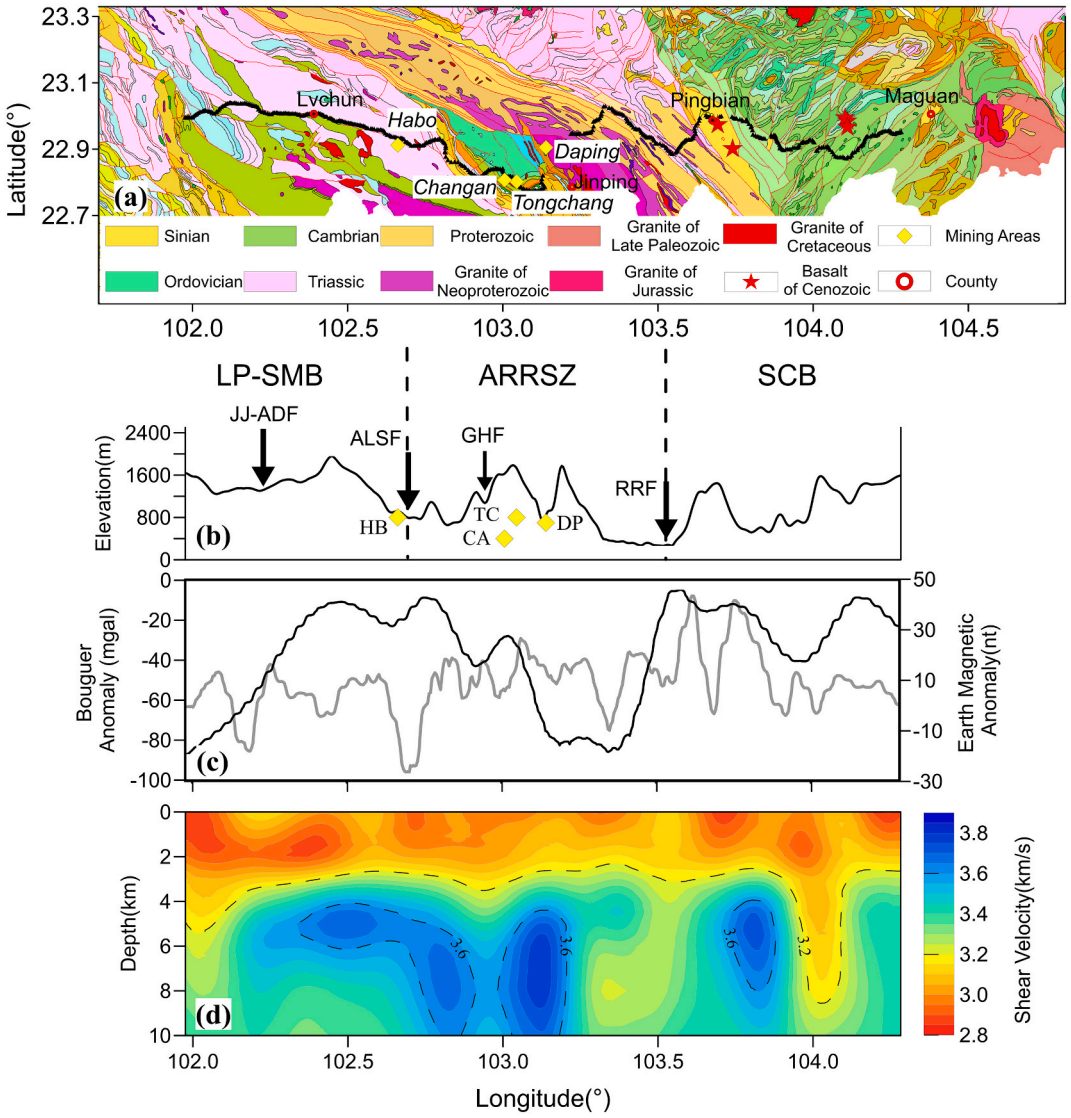

Fig. 13. (a) Geological map of the study area extracted from the geological map of Yunnan Province, China. (b) Elevation of the terrain; tectonic units, faults and ore deposits crossed by the reference profile (acronyms are the same as in Fig. 1). (c) Bouguer gravity anomaly (gray line, left axis) along the profile; data source: World Gravity Map (Bonvalot et al., 2012). Magnetic anomaly (black line, right axis) along the profile; data source: EMAG2 (Meyer et al., 2017). (d) Vertical shear velocity section (color scale on the right) along the virtual reference profile (numbers indicate velocity values in km/s).

2014a) and hence different lithological properties on both sides of the RRF. We believe that the difference revealed by our model is the manifestation of the structural boundary properties the RRF on scale of the upper crust.

The resolution of the proposed S-velocity model, achieved from the dense short-period array, allows us to distinguish two adjacent high- and low-velocity bodies east of the RRF (Fig. 13d). The resolution analysis, described in a previous section, has confirmed the ability of our data and survey array to recognize such scale anomalies. The high-velocity body is found beneath Pingbian, where the late-stage Cenozoic basalts occur, with outcrops on the surface (Fig. 13a). This high-velocity body is generally coincided with both the Bouguer anomaly and the magnetic anomaly at that location, both characterized by taking relatively high values (Fig. 13c). For the area of low velocity body, there are few studies. However, we noticed that it corresponds with falls in the Bouguer anomaly and the magnetic anomaly, and the topography at its location (Fig. 12) characterizes by a steep valley. At the same time, the valley is southwestward terminated at the RRF. Therefore, the low velocity is preliminarily interpreted to reflect a branch of the RRF, and thus they display similar features of low velocity. It should be noted that this interpretation is just based on the topographic data and needs further research to verify.

6.2. *Cenozoic magmatism in the ARRSZ and its adjacent areas*

As aforementioned, Cenozoic magmatism in the region can roughly be sorted into two stages, which were 42–24 Ma and < 17 Ma, respectively. The early stage is characterized by emplacement of alkali-rich porphyry granitoids intruding the southern part of the ARRSZ. These porphyry rocks, mainly consisting of granite-, quartz monazite- and syenite-porphyry, are temporally, spatially, and genetically related to the Cu-Au deposits. Studies have also attested that the granite porphyries and quartz monzonitic porphyries came from the partial melting of the thickened lower crust, while the syenite porphyries were generated from the enriched lithospheric mantle (Wu et al., 2019).

The late-stage magmatism occurred after 17 Ma characterized by the formation of basalts, such as those seen in the Pingbian area (Fig. 13a). These young basalts were originated from depths of 60–90 km (below the Moho) and were erupted less than 1.7 Ma ago (Huang et al., 2013b). This late-stage magmatic activity is interpreted to represent a response

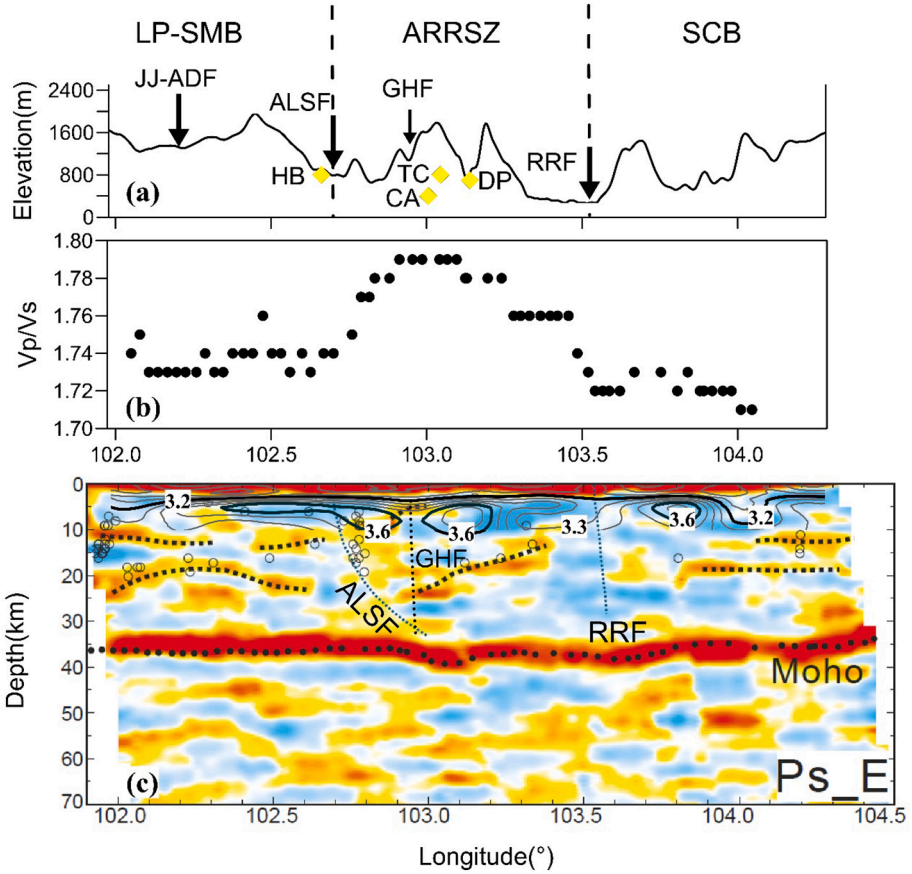

Fig. 14. (a) Elevation of the terrain; tectonic units, faults and ore deposits crossed by the reference profile (acronyms are the same as in Fig. 1). (b) Variation of the Vp/Vs ratio. (c) CCP stacking image obtained from receiver functions by Zhang et al. (2020a). The shear velocity model (values in km/s at depths of 2–10 km) is projected onto the top part of the image.

to the lateral flow of asthenospheric material beneath the Tibetan Plateau in the wake of the India-Eurasia collision.

Accordingly, we believe that our shear velocity model provides valuable information that can help better understand the Cenozoic magmatic activity and associated mineralization in the explored region. On the one hand, the high-velocity zone below the Ailaoshan metallogenic belt likely reflects buried granitoid intrusions. Considering the distribution of magmatic rocks in the region, we infer that these buried intrusions are probably early Cenozoic in age, similar to that of the granitoid porphyries currently exposed on the surface. Furthermore, these high velocity zones may also reflect the possible positions of potential Au-Cu mineralization because the mineral deposits in the area are closely related to granitoid intrusions. On the other hand, the high-velocity body near Pingbian might reflect the trace of the late-stage Cenozoic basalts. On the surface, these basalts are exposed in the Pingbian and Maguan areas, even in northern Vietnam (Huang et al., 2013b). Since no other magmatic intrusive bodies (e.g., granitoid intrusions) have been reported in the Pingbian area, we interpret this high-velocity body as indicative of existence of the intrusive phase of the younger basalts in the upper crust.

It is widely accepted that major faults (e.g., Ailaoshan Fault, Red River Fault) are normally as the ascending channels for magma and hydrothermal fluid and/or the sites for magma emplacement and ore mineral precipitation(He et al., 2008; Ying et al., 2006; Zhao et al., 2009). However, our model is limited to the upper crust scale, and cannot account for the Ailaoshan Fault because the seismic array runs partially parallel to its strike. Anyway, a clear distinguishing characteristic is the low velocity zone beneath the RRF indicating the weakened nature of rocks. This feature is probably due to two factors: one of them is ascribed to strong deformation of the fault and the other to the alteration of the rocks by fluids or hydrothermal processes along the fault. The CCP stacking image obtained from receiver functions using the same seismic array (Zhang et al., 2020a) gives us an in-depth view along the reference profile (Fig. 14c) that helps us to understand the role that these major faults played. The results provided by receiver functions suggest that these major faults could have acted as magmatic or hydrothermal channel during the magmatism and mineralization processes. Because the Cu-Au and/or polymetallic mineralization occurred during the early Cenozoic (ca. 44–24 Ma), we infer that it is mainly the early Cenozoic magmatic and ore-forming hydrothermal fluids that flowed up through these fault channels, to form the porphyries and associated Au-Cu and polymetallic deposits in the upper crust beneath the ARRSZ.

7. Conclusions

(1) We use the collected continuously recorded waveform data to apply ambient noise tomography and resolve a detailed upper crust image in the 2–10 km depth range in ARRSZ and its surroundings. The upper crust model shows a laterally varying S-velocity pattern alternating high and low velocities, and specifically reveals two high-velocity bodies in the upper crust: one of them lies mainly below the Ailaoshan metallogenic belt and the other, further east, beneath the Pingbian area. Both belts are separated by a low velocity zone near the RRF.

(2) The shear velocity model provides valuable information about the Cenozoic magmatism and associated mineralization in the region. The high-velocity body beneath the Ailaoshan

metallogenic belt probably corresponds to buried granitoid intrusions, which are the product of early-stage magmatism (42–24 Ma) and associated mineralization. Contrastingly, we interpret the high velocity body near Pingbian most likely to reflect the intrusive equivalents of the late-stage basalts (<17 Ma).

(3) The low velocity zone beneath RRF likely indicates the weakened nature of rocks below the RRF. Combining this with the results deduced from receiver functions using the same seismic array, we infer that the major regional faults – the Ailaoshan Fault and the Red River Fault – could have acted as magmatic or hydrothermal channels during the early Cenozoic magmatic and metallogenic activity.

CRediT authorship contribution statement

Mengjie Zheng: Formal analysis, Methodology, Software, Visualization, Writing - original draft. **Zhiming Bai:** Conceptualization, Investigation, Data curation, Project administration, Funding acquisition. **Tao Xu:** Conceptualization, Writing - review & editing, Supervision, Resources. **José Badal:** Writing - review & editing

Declaration of Competing Interest

The authors declare that they have no known competing financial interests or personal relationships that could have appeared to influence the work reported in this paper.

Acknowledgements

Thanks to the Short-period Seismic Array Laboratory of IGGCAS, Guiping Yu and Minfu Huang for their assistance in collecting the data used in this study. We appreciate the guidance, suggestions, and discussions with Profs. Laicheng Miao, Huajian Yao, Yingjie Yang, Yonghua Li and Yong Zheng. We are very grateful to the editor and two anonymous reviewers for their useful comments and suggestions that helped us improve the early manuscript. The present study was funded by the National Key Research and Development Project of China (2016YFC0600302, 2017YFC0601206), the Second Tibetan Plateau Scientific Expedition and Research Program (STEP) (2019QZKK0701), and the National Natural Science Foundation of China (41774097, 41674064, 41704042).

References

Badal, J., Chen, Y., Chourak, M., Stankiewicz, J., 2013. S-wave velocity images of the Dead Sea Basin provided by ambient seismic noise. J. Asian Earth Sci. 75, 26–35.

Bai, Z.M., Wang, C.Y., 2004. Tomography research of the Zhefang-Binchuan and Menglian-Malong wide-angle seismic profiles in Yunnan province. Chin. J. Geophys. 47, 257–267 (in Chinese).

Bao, X.W., Song, X.D., Li, J.T., 2015a. High-resolution lithospheric structure beneath mainland China from ambient noise and earthquake surface-wave tomography. Earth Planet. Sci. Lett. 417, 132–141.

Bao, X.W., Sun, X.X., Xu, M.J., Eaton, D.W., Song, X.D., Wang, L.S., Ding, Z.F., Mi, N., Li, H., Yu, D.Y., 2015b. Two crustal low-velocity channels beneath SE Tibet revealed by joint inversion of Rayleigh wave dispersion and receiver functions. Earth Planet. Sci. Lett. 415, 16–24.

Bensen, G.D., Ritzwoller, M.H., Barmin, M.P., Levshin, A.L., Lin, F., Moschetti, M.P., Shapiro, N.M., Yang, Y., 2007. Processing seismic ambient noise data to obtain reliable broad-band surface wave dispersion measurements. Geophys. J. Int. 169, 1239–1260.

Bonadio, R., Geissler, W.H., Lebedev, S., Fullea, J., Ravenna, M., Celli, N.L., Jokat, W., Jegen, M., Sens-Schönfelder, C., Baba, K.G., Geophysics, Geosystems, 2018. Hot upper mantle beneath the Tristan da Cunha hotspot from probabilistic Rayleigh-wave inversion and Petrological modeling. Geochem. Geophys. Geosyst. 19, 1412–1428.

Bonvalot, S., Balmino, G., Briais, A., Kuhn, M., Peyrefitte, A., Vales, N., Biancale, R., Gabalda, G., Reinquin, F., Sarrailh, M., 2012. World gravity map. In: Bureau Gravimetrique International (BGI), Map, CGMW-BGI-CNES728. IRD, Paris.

Cai, Y., Wu, J.P., Wang, W.L., Fang, L.H., Fan, L.P., 2016. S-wave velocity structure in the SE Tibetan plateau. Earthq. Sci. 29, 165–172.

Chung, S.-L., Lee, T.-Y., Lo, C.-H., Wang, P.-L., Chen, C.-Y., Yem, N.T., Hoa, T.T., Genyao, W., 1997. Intraplate extension prior to continental extrusion along the Ailao Shan-Red River shear zone. Geology 25, 311–314.

Chung, S.L., Lo, C.H., Lee, T.Y., Zhang, Y.Q., Xie, Y.W., Li, X., Wang, K.L., Wang, P.L., 1998. Diachronous uplift of the Tibetan plateau starting 40?Myr ago. Nature 394, 769–773.

Cong, Y., Dong, Q.J., Xiao, K.Y., 2013. Study on metallogenic model and ore exploration of porphyry deposits in Sanjiang metallogenic belt. J. Geol. 37, 562–569 (in Chinese).

Deng, W.M., Huang, X., Zhong, D.L., 1998a. Alkali-rich porphyries in the northern segment of the Jinshajiang belt, western Yunnan, and their relations to intraplate deformation. Sci. China Ser. D Earth Sci. 28, 111–117 (in Chinese).

Deng, W.M., Huang, X., Zhong, D.L., 1998b. Petrological characteristics and genesis of Cenozoic alkali-rich porphyry in west Yunnan, China. Sci. Geol. Sin. 33, 412–425 (in Chinese).

Ekström, G., Abers, G.A., Webb, S.C., 2009. Determination of surface-wave phase velocities across USArray from noise and Aki's spectral formulation. Geophys. Res. Lett. 36.

Fang, H.J., Yao, H.J., Zhang, H.J., Huang, Y.C., van der Hilst, R.D., 2015. Direct inversion of surface wave dispersion for three-dimensional shallow crustal structure based on ray tracing: methodology and application. Geophys. J. Int. 201, 1251–1263.

Fu, Y.V., Gao, Y., Li, A.B., Li, L., Chen, A.G., 2017. Lithospheric structure of the southeastern margin of the Tibetan plateau from Rayleigh wave tomography. J. Geophys. Res. Solid Earth 122, 4631–4644.

Gao, Y., Shi, Y.T., Wu, J., Tai, L.X., 2012. Shear-wave splitting in the crust: regional compressive stress from polarizations of fast shear-waves. Earthq. Sci. 25, 35–45.

Ge, L.S., Deng, J., Guo, X.D., Zou, Y.L., Liu, Y.C., 2009. Deep-seated structure and metallogenic dynamics of the Ailaoshan polymetallic mineralization concentration area, Yunnan Province, China. Sci. China Ser. D Earth Sci. 52, 1624.

Ge, L., Deng, J., Yang, L., Juan, S.S., Chunying, G., 2010. Evolution of tectonic environment and gold-polymetal metallogenic system in Ailaoshan ore concentration region, Yunnan Province, China. Acta Petrol. Sin. 26, 1699–1722 (in Chinese).

He, Z.H., Wang, Y., Mo, X.X., Zeng, P.S., Yu, X.H., Liu, H.L., 2008. Sources of ore foming materials in the Changan god deposit, Yunnan Province: evidence from the contents of ore foming elements in ore strata and magma from ore district. J. East China Univ. Technol. (Nat. Sci.) 3, 207–212 (in Chinese).

Hu, J.F., Su, Y.J., Zhu, X.G., Chen, Y., 2005. S-wave velocity and Poisson's ratio structure of crust in Yunnan and its implication. Sci. China Ser. D Earth Sci. 48, 210–218.

Huang, J.L., Zhao, D.P., Zheng, S.H., 2002. Lithospheric structure and its relationship to seismic and volcanic activity in Southwest China. J. Geophys. Res. Solid Earth 107, 2255.

Huang, H.-H., Xu, Z.J., Wu, Y.-M., Song, X.D., Huang, B.-S., 2013a. First local seismic tomography for Red River shear zone, northern Vietnam: stepwise inversion employing crustal P and Pn waves. Tectonophysics 584, 230–239.

Huang, X.K., Mo, X.X., Yu, X.H., Li, Y., He, W.Y., 2013b. Geochemical characteristics and geodynamic significance of Cenozoic basalts from Maguan and Pingbian, southeastern Yunnan Province. Acta Petrol. Sin. 29, 1325–1337 (in Chinese).

Huang, Y.-C., Lin, C.-H., Kagiyama, T., 2017. Shallow crustal velocities and volcanism suggested from ambient noise studies using a dense broadband seismic network in the Tatun volcano Group of Taiwan. J. Volcanol. Geotherm. Res. 341, 6–20.

Huang, Y.C., Ohkura, T., Kagiyama, T., Yoshikawa, S., Inoue, H., 2018. Shallow volcanic reservoirs and pathways beneath Aso caldera revealed using ambient seismic noise tomography. Earth Planets Space 70, 1–21.

Köhler, A., Weidle, C., Maupin, V., 2012. On the effect of topography on surface wave propagation in the ambient noise frequency range. J. Seismol. 16, 221–231.

Koulakov, I., Maksotova, G., Jaxybulatov, K., Kasatkina, E., Shapiro, N.M., Luehr, B.-G., El Khrepy, S., Al-Arifi, N., 2016. Structure of magma reservoirs beneath Merapi and surrounding volcanic centers of Central Java modeled from ambient noise tomography. Geochem. Geophys. Geosyst. 17, 4195–4211.

Lei, J.S., Zhao, D.P., Su, Y.J., 2009. Insight into the origin of the Tengchong intraplate volcano and seismotectonics in Southwest China from local and teleseismic data. J. Geophys. Res. Solid Earth 114.

Leloup, P.H., Lacassin, R., Tapponnier, P., Schärer, U., Zhong, D.L., Liu, X.H., Zhang, L.S., Ji, S.C., Trinh, P.T., 1995. The Ailao Shan-Red River shear zone (Yunnan, China), tertiary transform boundary of Indochina. Tectonophysics 251, 3–84.

Li, Y.H., Pan, J.T., Wu, Q.J., Ding, Z.F., 2014. Crustal and uppermost mantle structure of SE Tibetan plateau from Rayleigh-wave group-velocity measurements. Earthq. Sci. 27, 411–419.

Li, C., Yao, H.J., Fang, H.J., Huang, X.L., Wan, K.S., Zhang, H.J., Wang, K.D., 2016a. 3D near-surface shear-wave velocity structure from ambient-noise tomography and borehole data in the Hefei urban area, China. Seismol. Res. Lett. 87, 882–892.

Li, Z.W., Ni, S.D., Zhang, B.L., Bao, F., Zhang, S.Q., Deng, Y., Yuen, D.A., 2016b. Shallow magma chamber under the Wudalianchi volcanic field unveiled by seismic imaging with dense array. Geophys. Res. Lett. 43, 4954–4961.

Liang, H.Y., Campbell, Ian H., Allen, Charlotte M., Sun, W.D., Yu, H.X., Xie, Y.W., Zhang, Y.Q., 2007. The age of the potassic alkaline igneous rocks along the Ailao Shan–Red River shear zone: implications for the onset age of left-lateral shearing. J. Geol. 115, 231–242.

Liu, J., Tang, Y., Tran, M.-D., Cao, S., Zhao, L., Zhang, Z., Zhao, Z., Chen, W., 2012. The nature of the Ailao Shan–Red River (ASRR) shear zone: constraints from structural, microstructural and fabric analyses of metamorphic rocks from the Diancang Shan, Ailao Shan and Day Nui Con Voi massifs. J. Asian Earth Sci. 47, 231–251.

Liu, Y., Zhang, H.J., Fang, H.J., Yao, H.J., Gao, J., 2018. Ambient noise tomography of three-dimensional near-surface shear-wave velocity structure around the hydraulic

fracturing site using surface microseismic monitoring array. J. Appl. Geophys. 159, 209–217.
Liu, J., Chen, X., Tang, Y., Song, Z., Wang, W., 2019. The Ailao Shan–Red River shear zone revisited: timing and tectonic implications. GSA Bull. 132, 1165–1182.
Lou, H., Wang, C.Y., 2005. Wavelet analysis and interpretation of gravity data in Sichuan-Yunnan region, China. Acta Seismol. Sin. 18, 552–561 (in Chinese).
Luo, Y.H., Yang, Y.J., Xu, Y.X., Xu, H.R., Zhao, K.F., Wang, K., 2015. On the limitations of interstation distances in ambient noise tomography. Geophys. J. Int. 201, 652–661.
Ma, Q., Yang, Y., Zhao, Z.D., Tong, X., Wu, J., Miao, Z., Li, C., Lei, H., 2020. Titanite geochronology and geochemistry of the Cenozoic alkali-rich intrusions in the Ailaoshan -Red River Shear Zone, Yunnan Province. Acta Petrol. Sin. 36, 2751–2764 (in Chinese).
Matos, C., Silveira, G., Matias, L., Caldeira, R., Ribeiro, M.L., Dias, N.A., Krüger, F., Bento dos Santos, T., 2015. Upper crustal structure of Madeira Island revealed from ambient noise tomography. J. Volcanol. Geotherm. Res. 298, 136–145.
Meyer, B., Saltus, R., Chulliat, A., 2017. EMAG2: Earth magnetic anomaly grid (2-arc-minute resolution) version 3. In: National Centers for Environmental Information, NOAA. Model.
Peltzer, G., Tapponnier, P., 1988. Formation and evolution of strike-slip faults, rifts, and basins during the India-Asia collision: An experimental approach. J. Geophys. Res. 93, 15,085.
Ritzwoller, M.H., Levshin, A.L., 1998. Eurasian surface wave tomography: group velocities. J. Geophys. Res. Solid Earth 103, 4839–4878.
Roux, P., Moreau, L., Lecointre, A., Hillers, G., Campillo, M., Ben-Zion, Y., Zigone, D., Vernon, F., 2016. A methodological approach towards high-resolution surface wave imaging of the San Jacinto fault zone using ambient-noise recordings at a spatially dense array. Geophys. J. Int. 206, 980–992.
Sabra, K.G., Gerstoft, P., Roux, P., Kuperman, W.A., Fehler, M.C., 2005a. Extracting time-domain Green's function estimates from ambient seismic noise. Geophys. Res. Lett. 32.
Sabra, K.G., Roux, P., Kuperman, W.A., 2005b. Arrival-time structure of the time-averaged ambient noise cross-correlation function in an oceanic waveguide. J. Acoust. Soc. Am. 117, 164–174.
Schärer, U., Lian-Sheng, Z., Tapponnier, P., 1994. Duration of strike-slip movements in large shear zones: the Red River belt, China. Earth Planet. Sci. Lett. 126, 379–397.
Shapiro, N.M., Campillo, M., 2004. Emergence of broadband Rayleigh waves from correlations of the ambient seismic noise. Geophys. Res. Lett. 31.
Shearer, P.M., 2019. Introduction to Seismology. Cambridge university press.
Shi, Y.T., Gao, Y., Su, Y.J., Wang, Q., 2012. Shear-wave splitting beneath Yunnan area of Southwest China. Earthq. Sci. 25, 25–34.
Tapponnier, P., Peltzer, G., Le Dain, A.Y., Armijo, R., Cobbold, P., 1982. Propagating extrusion tectonics in Asia: new insights from simple experiments with plasticine. Geology 10, 611–616.
Tapponnier, P., Peltzer, G., Armijo, R., 1986. On the mechanics of the collision between India and Asia. Geol. Soc. Lond., Spec. Publ. 19, 113–157.
Tapponnier, P., Lacassin, R., Leloup, P.H., Schärer, U., Dalai, Z., Haiwei, W., Xiaohan, L., Shaocheng, J., Lianshang, Z., Jiayou, Z., 1990. The Ailao Shan/Red River metamorphic belt: tertiary left-lateral shear between Indochina and South China. Nature 343, 431–437.
Tian, G., Zhang, C.Q., Peng, H.J., Zhou, Y.M., Li, J.R., Zhang, X.P., Hu, M.Y., 2014. Petrogenesis and geodynamic setting of the Chang'an gold deposit in southern Ailaoshan metallogenic belt. Acta Petrol. Sin. 30, 125–138 (in Chinese).
Wang, J.H., Yin, A., Harrison, T.M., Grove, M., Zhang, Y.Q., Xie, G.H., 2001. A tectonic model for Cenozoic igneous activities in the eastern indo–Asian collision zone. Earth Planet. Sci. Lett. 188, 123–133.
Wang, C.Y., Chan, W.W., Mooney, W.D., 2003. Three-dimensional velocity structure of crust and upper mantle in southwestern China and its tectonic implications. J. Geophys. Res. Solid Earth 108, 2442.
Wang, C.Y., Chang, L.J., Ding, Z.F., Liu, Q.L., Liao, W.L., Flesch, L.M., 2014a. Upper mantle anisotropy and crust-mantle deformation pattern beneath the Chinese mainland. Sci. China Earth Sci. 57, 132–143.
Wang, F.Y., Pan, S.Z., Liu, L., Liu, B.F., Zhang, J.S., Deng, X.G., Ma, C.J., Zhang, C.J., 2014b. Wide angle seismic exploration of Yuxi-Lincang profile-The research of crustal structure of the red river fault zone and southern Yunnan. Chin. J. Geophys. 57, 3247–3258 (in Chinese).
Wang, Y., Lin, F.-C., Schmandt, B., Farrell, J., 2017. Ambient noise tomography across Mount St. Helens using a dense seismic array. J. Geophys. Res. Solid Earth 122, 4492–4508.
Wen, L.M., Kang, G.F., Bai, C.H., Gao, G.M., Zheng, A.R., An, B.L., 2017. Crustal magnetic anomalies and geological structure in the Yunnan region. Chin. J. Geophys. 60, 613–626 (in Chinese).
Wu, J.K., Zhao, Z.D., Yang, Y.Y., Lei, H.S., Miao, Z., Liu, D., Zhu, D.C., Yu, X.H., 2019. Petrogenesis and geological implications of the alkali-rich porphyry in southern Ailaoshan-Red River shear zone. Acta Petrol. Sin. 35, 485–504 (in Chinese).
Xu, Y., Liu, J.H., Liu, F.T., Song, H.B., Hao, T.Y., Jiang, W.W., 2005. Crust and upper mantle structure of the Ailao Shan-Red River fault zone and adjacent regions. Sci. China Ser. D Earth Sci. 48, 156–164.
Xu, B., Hou, Z.-Q., Griffin, W.L., Zheng, Y.-C., Wang, T., Guo, Z., Hou, J., Santosh, M., O'Reilly, S.Y., 2020. Cenozoic lithospheric architecture and metallogenesis in southeastern Tibet. Earth Sci. Rev. 103472.
Yang, Z., Yin, J., Sun, Z., Otofuji, Y.-I., Sato, K., 2001. Discrepant cretaceous paleomagnetic poles between eastern China and Indochina: a consequence of the extrusion of Indochina. Tectonophysics 334, 101–113.
Yang, H.Y., Peng, H.C., Hu, J.F., 2017. The lithospheric structure beneath Southeast Tibet revealed by P and S receiver functions. J. Asian Earth Sci. 138, 62–71.
Yao, H.J., Xu, G.M., Zhu, L.B., Xiao, X., 2005. Mantle structure from inter-station Rayleigh wave dispersion and its tectonic implication in western China and neighboring regions. Phys. Earth Planet. Inter. 148, 39–54.
Yao, H.J., van Der Hilst, R.D., de Hoop, M.V., 2006. Surface-wave array tomography in SE Tibet from ambient seismic noise and two-station analysis — I. phase velocity maps. Geophys. J. Int. 166, 732–744.
Yao, H., Gouédard, P., Collins, J.A., McGuire, J.J., van der Hilst, R.D., 2011. Structure of young East Pacific rise lithosphere from ambient noise correlation analysis of fundamental- and higher-mode Scholte-Rayleigh waves. Compt. Rendus Geosci. 343, 571–583.
Ying, H.L., Liu, H.L., Yang, X.Z., Li, Z.W., 2006. Geology and origin of Tongchang gold deposit in Yunnan province. Geol. Resour. 15, 265–271 (in Chinese).
Yuan, S.S., Ge, L.S., Lu, Y.M., Guo, X.D., Wang, M.J., Wang, Z.H., Zou, Y.L., 2010. Relationship between crust–mantle reaction and gold mineralization in Ailaoshan metallogenic belt: a case study of Daping gold deposit in Yuanyang. Mineral Deposits 29, 253–264 (in Chinese).
Zhang, Z., Zhao, B., Zhang, X., Liu, C., 2006. Crustal structure beneath the wide-angle seismic profile between Simao and Zhongdian in Yunnan. Chin. J. Geophys. 49, 1377–1384 (in Chinese).
Zhang, X.M., Hu, J.F., Hu, Y.L., Yang, H.Y., Chen, J., Peng, H.C., Wen, L.M., 2011. The S-wave velocity structure in the crust and upper mantle as well as the tectonic setting of strong earthquake beneath Yunnan region. Chin. J. Geophys. 54, 1222–1232 (in Chinese).
Zhang, L., Bai, Z.M., Xu, T., Wu, Z.B., Huang, M.F., Yu, G.P., Chen, J.L., Zheng, M.J., 2020a. Cenozoic magmatic activity and oblique uplifting of the Ailao Mountain: evidence from a short-period dense seismic array. Sci. China Earth Sci. 63, 1294–1308.
Zhang, M.H., Wu, Z.B., Ma, L.X., Zheng, F., Xie, T.T., Zheng, M.J., Hou, J., Liu, Y.S., Zhang, Y.Q., Xu, T., Bai, Z.M., 2020b. Research progress of passive source detection technology based on short-period dense seismic array. Prog. Geophys. 35, 495–511 (in Chinese).
Zhao, D.K., Wang, M.S., Xue, H.Y., Fang, M., Xia, G.T., 2009. Geological properties and genesis analysis on Habo gold deposit in Yuanyang of Yunan. J. Geol. 33, 230–234 (in Chinese).
Zheng, D.C., Ge, Z.X., Yang, R.H., Min, Z.X., Tang, Y.C., Jiang, M.M., Pang, W.D., 2014. Broadband ambient noise tomography in Yunnan Province. Acta Seismol. Sin. 36, 602–614 (in Chinese).
Zhu, X.P., Mo, X.X., White, N.C., Zhang, B., Sun, M.X., Wang, S.X., Zhao, S.L., Yang, Y., 2009. Geology and metallogenetic setting of the Habo porphyry Cu (Mo-Au) deposit, Yunnan. Acta Geol. Sin. 83, 1916–1928 (in Chinese).